

# Crystallization pathways, morphologies and structural defects of $\alpha$ -MnO<sub>2</sub> nanomaterial synthesized under annealed temperatures

**Van-Phuc Dinh**

Institute of Fundamental and Applied Sciences, Duy Tan University <https://orcid.org/0000-0002-2956-3398>

**Anh Tuyen Luu**

Center for Nuclear Technology, Vietnam Atomic Energy Institute

**Siemek Krzysztof**

Dzheleпов Laboratory of Nuclear Problems, JINR

**Denis Kozlenko**

Joint Institute for Nuclear Research

**Le Khiem**

Institute of Physics, Vietnam Academy of Science and Technology

**Nguyen Toan Dang**

Institute of Research and Development, Duy Tan University

**Van Tiep Nguyen**

Institute of Physics, Viet Nam Academy of Science and Technology

**Le-Phuc Nguyen**

Vietnam Petroleum Institute

**Duy Tap Tran**

Faculty of Materials Science and Technology, University of Science, VNU–HCMC

**Trong Phuc Phan**

Center Nuclear Technologies, Vietnam Atomic Energy Institute

**Thai Son Lo**

Center Nuclear Technologies, Vietnam Atomic Energy Institute

**Tuan Kiet Hoang Anh**

Institute of Research and Development, Duy Tan University

**Thanh Khan Dinh**

University of Science and Education, The University of Da Nang

**Thuy Ngoc Luong**

Vietnam Petroleum Institute

**Ngoc-Chung Le**

DaLat University, Dalat University

**Ngoc-Tuan Nguyen**

DaLat University, Dalat University

**Thien-Hoang Ho**

Dong Nai University

**Dong Xuan Tran**

Institute of Fundamental and Applied Sciences, Duy Tan University

**Quang Hung Nguyen** (✉ [nguyenquanghung5@duytan.edu.vn](mailto:nguyenquanghung5@duytan.edu.vn))

Duy Tan University <https://orcid.org/0000-0002-9739-301X>

---

## Article

**Keywords:** a-MnO<sub>2</sub>, inorganic nanomaterials, crystallization pathways, morphologies, structural defects

**Posted Date:** September 1st, 2020

**DOI:** <https://doi.org/10.21203/rs.3.rs-63319/v1>

**License:** © ⓘ This work is licensed under a Creative Commons Attribution 4.0 International License.

[Read Full License](#)

---

# Crystallization pathways, morphologies and structural defects of $\alpha$ -MnO<sub>2</sub> nanomaterial synthesized under annealed temperatures

Van-Phuc Dinh<sup>1,2,\*</sup>, L. Anh Tuyen<sup>3,4,\*</sup>, K. Siemek<sup>4,5</sup>, D. P. Kozlenko<sup>6</sup>, L. Hong Khiem<sup>7,8</sup>, N. T. Dang<sup>9,2</sup>, N. Van Tiep<sup>7,10</sup>, Le-Phuc Nguyen<sup>11</sup>, Tran Duy Tap<sup>12,13</sup>, P. Trong Phuc<sup>3</sup>, L. Thai Son<sup>3</sup>, H. A. Tuan Kiet<sup>9,14</sup>, D. Thanh Khan<sup>15</sup>, Thuy Ngoc Luong<sup>11</sup>, Ngoc-Chung Le<sup>16</sup>, Ngoc-Tuan Nguyen<sup>17</sup>, Thien-Hoang Ho<sup>18</sup>, T. Dong Xuan<sup>1,2</sup>, N. Quang Hung<sup>1,2,\*</sup>

<sup>1</sup>*Institute of Fundamental and Applied Sciences, Duy Tan University, Ho Chi Minh City 700000, Viet Nam*

<sup>2</sup>*Faculty of Natural Sciences, Duy Tan University, Da Nang City 550000, Viet Nam*

<sup>3</sup>*Center Nuclear Technologies, Vietnam Atomic Energy Institute, Ho Chi Minh City 700000, Viet Nam*

<sup>4</sup>*Dzhelepov Laboratory of Nuclear Problems, JINR, 141980 Dubna, Moscow Reg., Russia*

<sup>5</sup>*Institute of Nuclear Physics, Polish Academy of Sciences, PL-31342 Krakow, Poland*

<sup>6</sup>*Frank Laboratory of Neutron Physics, JINR, 141980 Dubna, Moscow Reg., Russia*

<sup>7</sup>*Institute of Physics, Viet Nam Academy of Science and Technology, 10 Dao Tan, Ba Dinh, Ha Noi City 100000, Viet Nam*

<sup>8</sup>*Graduate University of Science and Technology, Vietnam Academy of Science and Technology, 18 Hoang Quoc Viet, Ha Noi City 100000, Viet Nam*

<sup>9</sup>*Institute of Research and Development, Duy Tan University, Da Nang City 550000, Viet Nam*

<sup>10</sup>*Flerov Laboratory of Nuclear Reactions, JINR, 141980 Dubna, Moscow Reg., Russia*

<sup>11</sup>*Vietnam Petroleum Institute, Ho Chi Minh City 700000, Viet Nam*

<sup>12</sup>*Faculty of Materials Science and Technology, University of Science, VNU-HCMC, 227 Nguyen Van Cu, District 5, Ho Chi Minh City 700000, Viet Nam*

<sup>13</sup>*Vietnam National University Ho Chi Minh City, Ho Chi Minh City 700000, Viet Nam*

<sup>14</sup>*Graduate School of Education, University of Pennsylvania, Philadelphia, Pennsylvania 19104, USA*

<sup>15</sup>*University of Science and Education, The University of Da Nang, Da Nang City 550000, Viet Nam*

<sup>16</sup>*DaLat University, Dalat University, 01 Phu Dong Thien Vuong, Da Lat City 670000, Viet Nam*

<sup>17</sup>*Dalat Nuclear Research Institute, 01 Nguyen Tu Luc, Da Lat City 670000, Viet Nam*

<sup>18</sup>*Dong Nai University, Le Quy Don Street, Bien Hoa City, Dong Nai 810000, Viet Nam*

Corresponding author: [dinhvanphuc@duytan.edu.vn](mailto:dinhvanphuc@duytan.edu.vn); [tuyenluuanh@gmail.com](mailto:tuyenluuanh@gmail.com); [nguyenquanghung5@duytan.edu.vn](mailto:nguyenquanghung5@duytan.edu.vn)

Manganese dioxide, in particular  $\alpha$ -MnO<sub>2</sub>, is one of the advanced inorganic nanomaterials having wide applications in many areas. Hence, understanding the crystallization pathways, morphologies, and formation mechanism of defects in its structure is of particular importance, not only for fundamental science but also for practical applications. Herein, different physically and chemically based methods, such as Neutron Diffraction (ND), XRD, SEM, TPR- H<sub>2</sub>, TGA-DSC, FT-IR, Positron Annihilation Lifetime (PAL), Doppler Broadening (DB) of positron annihilation radiation, and Electron-Momentum Distribution (EMD) measurements combined with theoretical calculations, were utilized to systematically investigate the composition, structure, and morphology of  $\alpha$ -MnO<sub>2</sub> nanomaterial under different annealed temperatures. The investigated material was synthesized at room temperature using a facile chemical method with potassium permanganate (KMnO<sub>4</sub>) and ethanol (C<sub>2</sub>H<sub>5</sub>OH), prior to being treated by temperatures of 100 °C – 800 °C. Results demonstrated, for the first time, that the  $\alpha$ -MnO<sub>2</sub>

50 nucleation can be formed even at room temperature and gradually developed to  $\alpha$ -MnO<sub>2</sub>  
51 nanorods at 600 °C. This novel finding, which cannot be explored by conventional XRD,  
52 was confirmed by ND analysis. In addition, PAL analysis combined with theoretical *ab*  
53 *initio* calculations indicated the existence of H<sup>+</sup> ions in the tunnel [1x1] of  $\alpha$ -MnO<sub>2</sub>. At the  
54 same time, DB and EMD measurements explored the presence of Mn and O vacancies in  
55  $\alpha$ -MnO<sub>2</sub> crystals at low temperatures. Finally, the present study reported a remarkable  
56 finding that organic molecules may act as reactants as well as templates, which are  
57 entirely decomposed and disappeared at highly annealed temperatures.

58 Understanding the crystallization pathways plays a key role in controlling the morphology  
59 and structure of nanomaterials. This will create suitable synthesized materials for applications  
60 in different areas. Manganese dioxide (MnO<sub>2</sub>) in its nanostructure is one of the advanced  
61 inorganic materials having wide applications in dry-cell batteries<sup>1</sup>, catalytic oxidation<sup>2</sup>, ion-  
62 exchange<sup>3</sup>, molecular adsorption<sup>4</sup>, solar energy conversion<sup>5</sup>, etc. Generally, MnO<sub>2</sub> consists of  
63 5 crystallographic  $\alpha$ ,  $\beta$ ,  $\gamma$ ,  $\delta$ , and  $\lambda$  structures<sup>6</sup>, among which  $\alpha$ -MnO<sub>2</sub> is well-known as a  
64 precursor material commonly used in electrochemical sensors<sup>7</sup>, catalysts<sup>8</sup>, cathodes of lithium  
65 or Mg batteries<sup>9,10</sup> and molecular sieves<sup>11</sup>, owing to its unique physical and chemical properties.

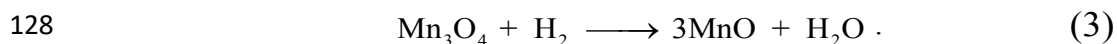
66 In order to investigate the morphology, structure, and specific properties of MnO<sub>2</sub>  
67 nanomaterials, many physical and chemical methods have been applied. Common physical  
68 methods are powder X-ray diffraction (PXRD), electron microscope (SEM or TEM), infrared  
69 spectroscopy (IR), and Raman scattering, whereas regular chemical methods include thermal  
70 gravimetric analysis and differential scanning calorimeter (TGA-DSC), surface area and porous  
71 size (BET-BJH) analysis, and temperature-programmed reduction (TPR). Although physical  
72 methods have been popularly used to study the structure and chemical bonding of  
73 nanomaterials, they are not effective in determining the material components as well as defects  
74 and porous structures existing outside the material framework under different crystallization  
75 conditions<sup>12,13</sup>. Similarly, chemical methods, which are often used to measure the phase  
76 transitions and porous components of materials, cannot exactly determine chemical components  
77 of the materials having multi-oxidations as manganese (Mn)<sup>12,14,15</sup>.

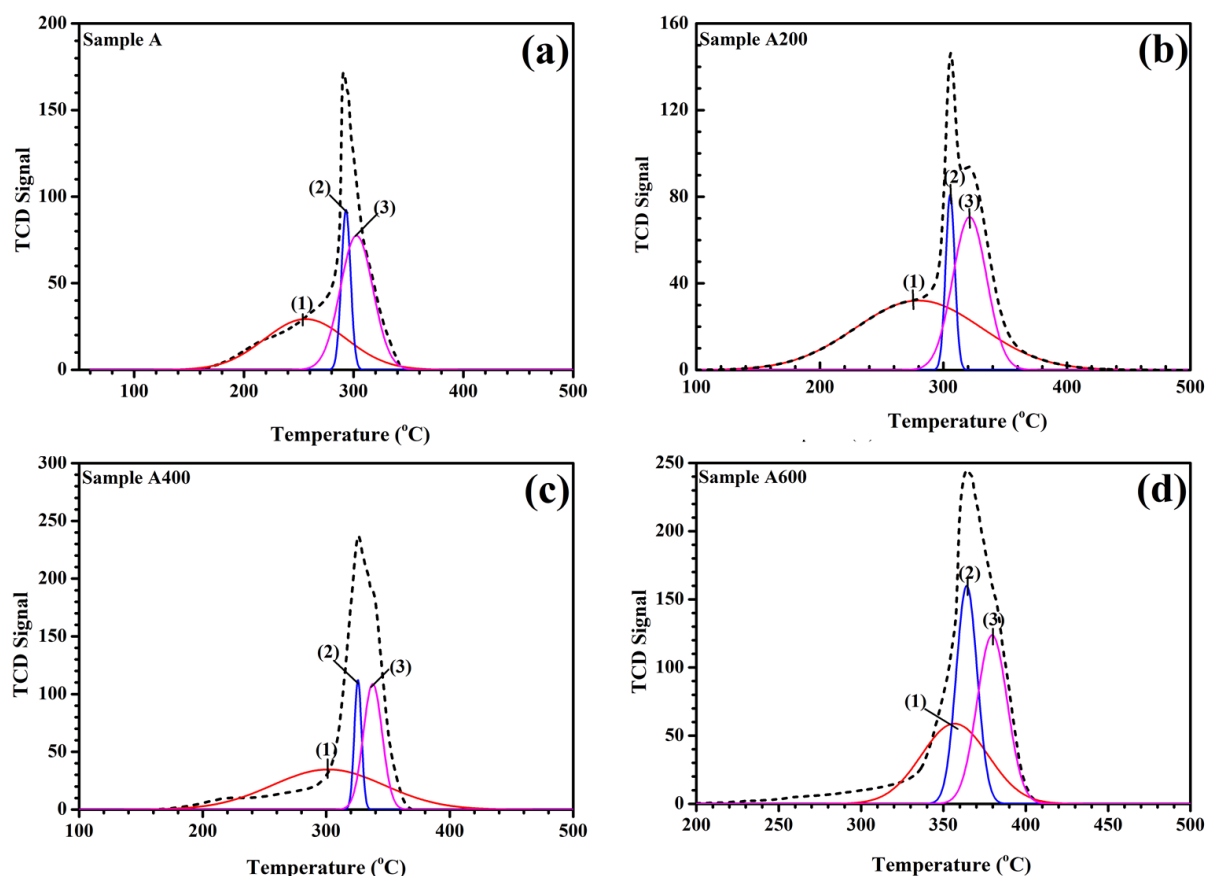
78 Regarding the synthesis process, various methods have been applied to synthesize  $\alpha$ -MnO<sub>2</sub>,  
79 such as thermal decomposition<sup>16,17</sup>, chemical method<sup>1</sup>, sol-gel method<sup>18,19</sup>, hydrothermal  
80 method<sup>20,21</sup>, microwave technique<sup>22</sup>, etc. Among them, hydrothermal methods are mostly  
81 preferred due to their simple operation and ability to obtain large and high-quality crystals while  
82 maintaining reasonable control of their shape and chemical composition<sup>20</sup>. Sol-gel methods are  
83 sometimes used because of their simple, homogenous, reliable, reproductive, and controllable  
84 features<sup>18</sup>. Both methods, however, are facing problems with high fabrication cost and long  
85 decomposition time<sup>23</sup>. This problem can be solved using chemical methods, owing to their  
86 simplicity, low cost, quick preparation, and easy-to-control both particle size and material  
87 composition<sup>24</sup>. For instance, Subramanian *et al.* reported that MnO<sub>2</sub> agglomerated nanosheets  
88 and nanowhiskers can be formed via a reaction between KMnO<sub>4</sub> and different alcohols such as  
89 ethanol, methanol, and pentanol<sup>25</sup>. However, crystalline structures of these materials as well as  
90 their crystallization pathways were not determined. Using the same reaction, Chodankar *et al.*  
91 synthesized  $\alpha$ -MnO<sub>2</sub> thin films and studied their formation mechanism based on an idea of  
92 nucleation<sup>26</sup>. Nevertheless, the nucleation structure and crystallization pathways of  $\alpha$ -MnO<sub>2</sub>  
93 were not investigated. Recently, by combining experimental methods with theoretical studies,  
94 Chen *et al.* have indicated the effects of potassium ion concentrations on different

95 crystallization pathways of  $\alpha$ -MnO<sub>2</sub> synthesized by using the hydrothermal method<sup>27</sup>. In fact,  
96 the  $\alpha$ -MnO<sub>2</sub> crystallization pathways were proposed based on an introduction of multistage  
97 nucleation, but such a nucleation stage has never been observed and/or determined so far.  
98 Furthermore, the effect of ions on the characteristic tunnels of nanostructured  $\alpha$ -MnO<sub>2</sub> has not  
99 also been reported.

100 In the present study, we combine, for the first time, different physical, chemical, and  
101 nuclear analytical methods together with theoretical calculations in order to have a  
102 comprehensive understanding on the crystallization pathways of nanostructured  $\alpha$ -MnO<sub>2</sub>  
103 formed via a reaction between ethanol and KMnO<sub>4</sub>, in which effects of temperature and reactant  
104 on the formation of  $\alpha$ -MnO<sub>2</sub> crystalline structure will be studied in detail. In particular, the  
105 nucleation of  $\alpha$ -MnO<sub>2</sub> occurred even at the room temperature will be demonstrated, whereas  
106 the impact of ions on the characteristic tunnels of  $\alpha$ -MnO<sub>2</sub> as well as the structural defects  
107 existed inside the material will be also discussed.

108 **TPR-H<sub>2</sub> analysis.** **Supplementary Fig. 1** shows the TPR-H<sub>2</sub> profiles of the A, A200, A400,  
109 and A600 samples. It is worth mentioning that the reduction of MnO<sub>2</sub>, in general, should be  
110 proceeded through three stages<sup>18,19,26,28</sup>. First, MnO<sub>2</sub> is converted to Mn<sub>2</sub>O<sub>3</sub> (**Eq. 1**). Second,  
111 Mn<sub>2</sub>O<sub>3</sub> is changed to Mn<sub>3</sub>O<sub>4</sub> (**Eq. 2**) and finally reduced to MnO as temperature reaches the  
112 highest value (**Eq. 3**). All TPR profiles in **Supplementary Fig. 1** are deconvoluted using the  
113 peak fit 4.12 program with Gaussian-type functions and the results are presented in **Fig. 1**. It  
114 can be seen that the reduction temperature of MnO<sub>x</sub> increases with increasing the annealed  
115 temperature. This observation suggests a subsequent increase in the size of MnO<sub>x</sub> particles with  
116 increasing temperature. When temperature is low as in the A and A200 samples, the size of  
117 MnO<sub>x</sub> particles is rather small and the endothermic reaction requires low energy only. Those  
118 small particles tend to coagulate to form crystals and/or nanorods. As temperature is high as in  
119 the A400 and A600 samples, higher energy consumption is required for the endothermic  
120 reaction to be occurred. This feature entirely agrees with those seen in the SEM images in **Fig.**  
121 **2**. Moreover, the calculated H<sub>2</sub> uptakes are found to be similar for all samples (around 1.1 x 10<sup>3</sup>  
122  $\mu\text{mol.g}^{-1}$ ) as indicated in **Supplementary Table 1**. Taking into account the H<sub>2</sub> consumption in  
123 a temperature range of 100 °C-500 °C, a mean oxidation state of 4 is obtained for Mn in all  
124 studied samples. The above TPR-H<sub>2</sub> results, therefore, clearly indicate that all studied samples  
125 used in the present work are pure and have the same chemical formula to be MnO<sub>2</sub>.

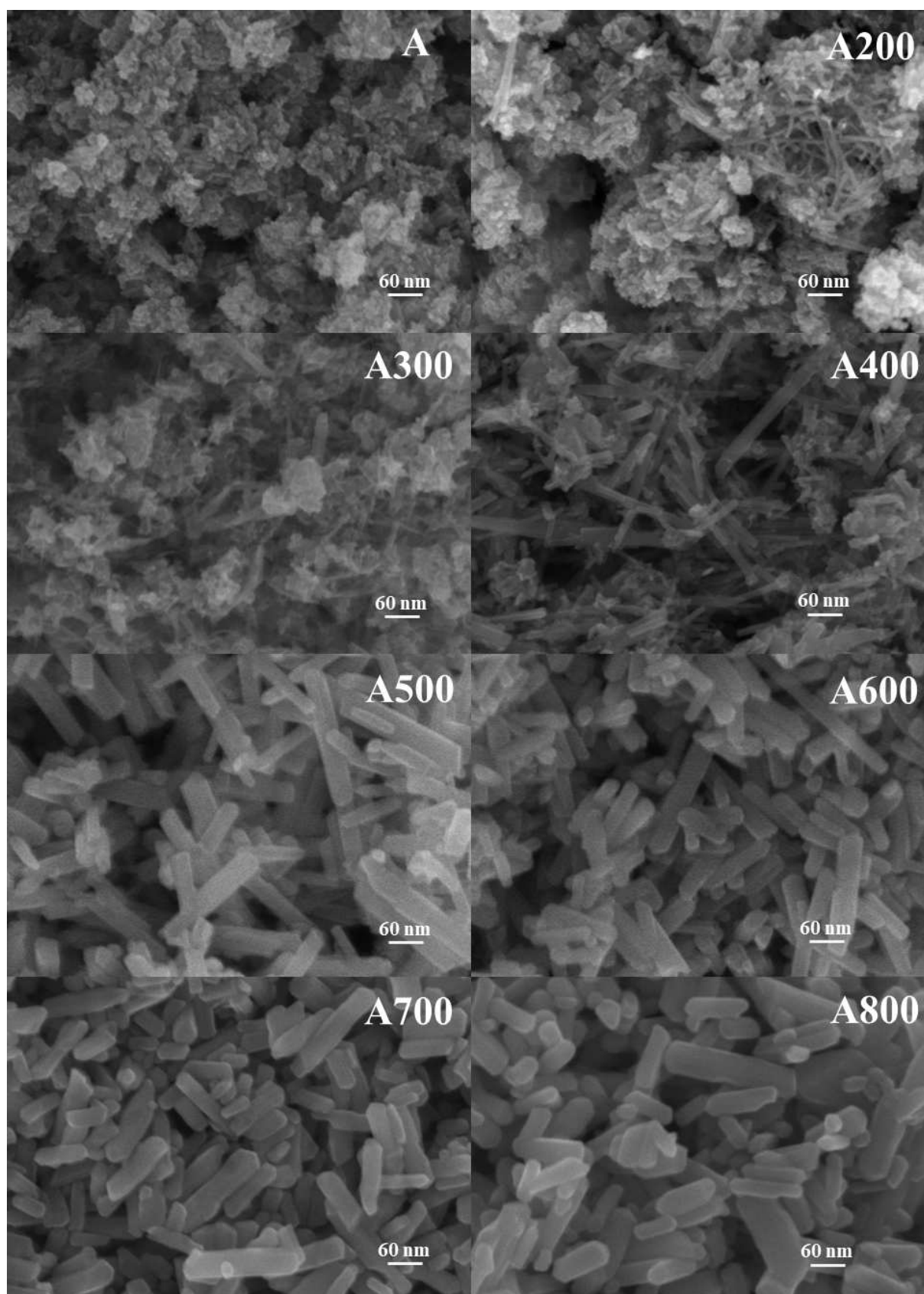




129

130 **Fig. 1. TPR-H<sub>2</sub> profiles of different MnO<sub>x</sub> samples according to three stages: (1) MnO<sub>2</sub>**  
 131 **→ Mn<sub>2</sub>O<sub>3</sub>, (2) Mn<sub>2</sub>O<sub>3</sub> → Mn<sub>3</sub>O<sub>4</sub>, and (3) Mn<sub>3</sub>O<sub>4</sub> → MnO.**

132 **SEM analysis.** SEM images of all studied samples are shown in **Fig. 2**. It is seen that the A  
 133 sample has a porous surface with a large number of small particles. Some short nanowires  
 134 similar to corals were formed in this sample. At 200 °C (A200 sample), these particles seem to  
 135 be clumped, suggesting a decrease in the material's surface area. The nanowires are then  
 136 noticeably grown above this temperature. At 400 °C, a heterogeneous surface structure  
 137 including nucleation and nanorods is seen (A400 sample). Hence, temperature directly affects  
 138 the development of α-MnO<sub>2</sub> crystalline structure from nucleation to nanorods. Above 500 °C,  
 139 α-MnO<sub>2</sub> nanorods reach their complete structure, which can be seen via the XRD patterns in  
 140 **Fig. 4a** and extracted unit cell sizes in **Supplementary Table 2**.



141

142

**Fig. 2. SEM images of all studied samples at different annealed temperatures.**

143

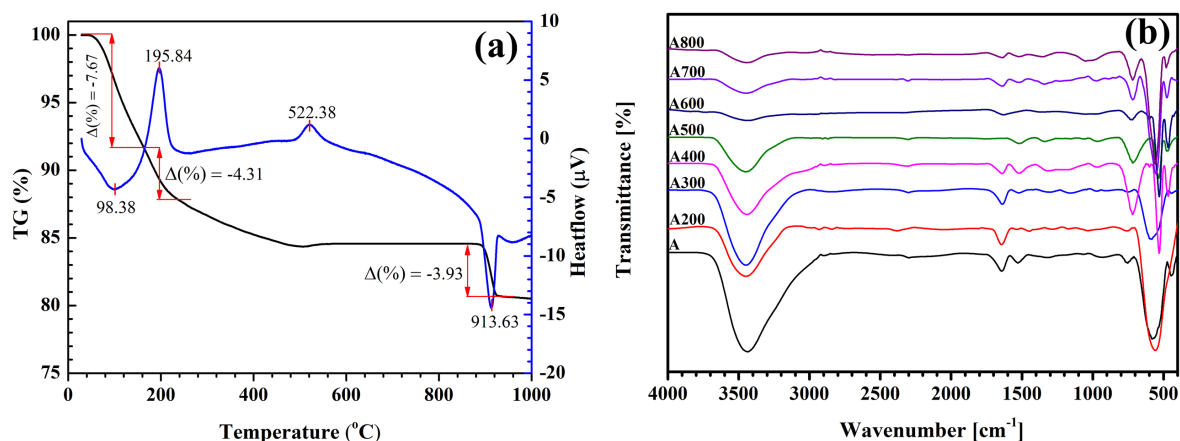
144

145

146

**TGA-DSC analysis.** TGA-DSC analysis was carried out (in the atmosphere) for the A sample and the results are depicted in **Fig. 3a**. This figure shows two endothermic and two exothermic processes when temperature increases from 40 °C to 1000 °C. Obviously, there is a low endothermic peak at 98.38 °C related to the loss of absorbed water molecules and organic

147 compounds under synthesis conditions with a weight loss of about 7.67%. The second  
 148 endothermic peak corresponding to the melting with a weight loss of nearly 3.93% is recorded  
 149 at 913.63 °C. An exothermic peak at 195.84 °C, which corresponds to the decomposition of  
 150 alkyl groups with a weight loss of approximately 4.31%, is also observed. Another exothermic  
 151 peak seen at 522.38 °C is attributed to the crystallization as the associated weight loss is almost  
 152 zero. Hence, it can be concluded here that alkyl groups have contributed to the formation of  
 153 MnO<sub>2</sub> structure but they disappear as temperature becomes higher than 200 °C, prior to the  
 154 crystallization of α-MnO<sub>2</sub> at 522.38 °C.



155

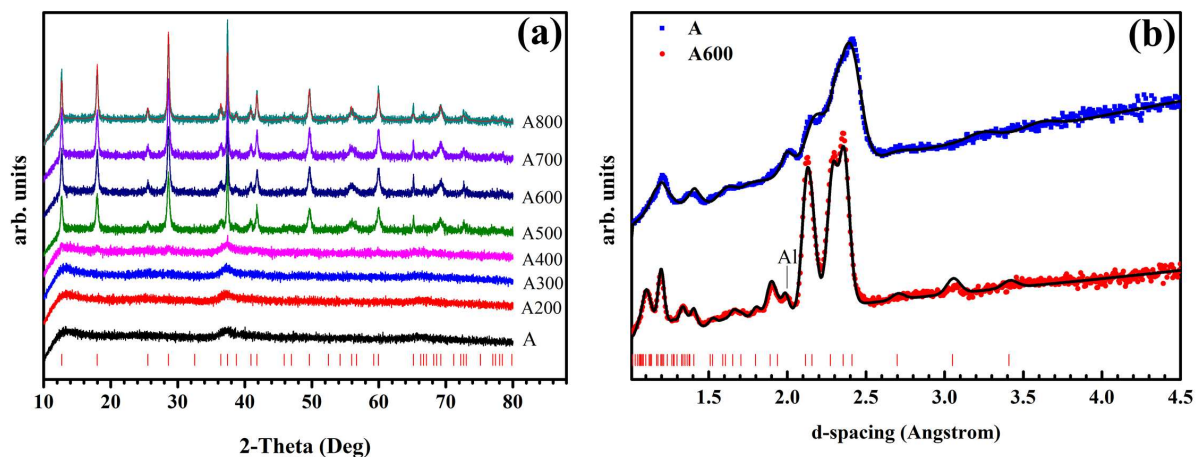
156 **Fig. 3. TGA-DSC of MnO<sub>2</sub> powder (A sample) in air (a) and FT-IR spectra of MnO<sub>2</sub>**  
 157 **samples (b)**

158 **FT-IR spectroscopy.** FT-IR spectra of all samples recorded in a wavenumber range of 4000  
 159 cm<sup>-1</sup> – 400 cm<sup>-1</sup> are shown in **Fig. 3b**. Spectra of A, A200, A300, and A400 samples have two  
 160 sharp specific peaks at approximately 3400 cm<sup>-1</sup> and 1600 cm<sup>-1</sup>, which are related to –O–H  
 161 group of alcohol and C=O bond in carbonyl group of aldehydes, respectively. These peaks  
 162 completely disappear above 500 °C. Some peak shifts associated with Mn–O bonds from 580  
 163 cm<sup>-1</sup> to nearly 530 cm<sup>-1</sup> when temperature rises from 100 °C to 400 °C are clearly observed.  
 164 These interesting peak shifts can be interpreted as follows. Under the synthetic conditions,  
 165 oxygen atoms in unit cells of [MnO<sub>6</sub>] can interact with manganese atoms and alkyl groups,  
 166 similar to those obtained from the TGA-DSC analysis in **Fig. 3a**. With increasing temperature,  
 167 the decomposition of alkyls occurs, resulting in a reduction of the bonding length of Mn–O,  
 168 which completely agrees with the reduction of unit cell sizes detected by the XRD patterns in  
 169 **Fig. 4a**. These results consequently lead to a shift of the wavenumber around the 580 cm<sup>-1</sup> peak.

170 **XRD analysis.** XRD spectra presented in **Fig. 4a** show that the peak intensities of A, A200,  
 171 A300, and A400 samples are rather low and no specific peak of MnO<sub>2</sub> crystallinity is seen in  
 172 these samples. The remain samples (from A500 to A800) clearly exhibit intensive characteristic  
 173 peaks of α-MnO<sub>2</sub> with a pure tetragonal phase (JCPDS no. 44-0141) observed at 2θ = 13.17,  
 174 18.71, 26.73, 29.96, 38.24, 39.31, 40.73, 45.21, 47.90, 54.58, 58.81, 64.30, 68.41, and 72.26  
 175 degrees. These diffraction angles are associated with (110), (200), (220), (310), (400), (211),  
 176 (301), (510), (411), (600), (521), (002), (541), and (312) diffraction planes, indicating that there  
 177 should be no crystalline phase existed in the A, A200, A300, and A400 species. This result is  
 178 absolutely consistent with the above TGA-DSC analysis for the crystallization at 522.38 °C.  
 179 However, SEM images in **Fig. 2** reveal a completely different behavior, namely the  
 180 crystallization gradually occurred to form nanowires as temperature is varied from 100 °C to  
 181 400 °C (**Figs. 2a-2d**). This contradiction between XRD analysis and SEM pictures can be  
 182 explained by the fact that the α-MnO<sub>2</sub> nucleation together with α-MnO<sub>2</sub> crystals with relatively

183 small size have been possibly formed at room temperature, prior to growing to  $\alpha$ -MnO<sub>2</sub>  
 184 nanorods as temperature is increased. This phenomenon can be confirmed by using the ND  
 185 analysis presented in **Fig. 4b**.

186 **ND analysis.** **Fig. 4b** shows the ND patterns of A and A600 samples. The presence of broad  
 187 diffraction peaks in the A sample is clearly observed, which indicates the formation of  
 188 nanoparticles. The positions of these peaks at the  $d$ -spacings around 1.2 Å, 2.15 Å and 2.4 Å  
 189 can be associated with the tetragonal crystalline structure of  $\alpha$ -MnO<sub>2</sub>. In the diffraction patterns  
 190 of A600 sample, the diffraction peaks become better resolved. They can be assigned to the  
 191 characteristic reflections of  $\alpha$ -MnO<sub>2</sub> crystals at  $d$ -spacings ( $h, k, l$ ) of 1.11 Å (8, 1, 1), 1.19 Å  
 192 (3, 2, 3), 1.89 Å (5, 1, 0), 2.11 Å (0, 3, 1), and a strong double peak corresponding to the  
 193 reflection (3 3 0) at 2.27 Å and (1 2 1)/(2 1 1) at 2.35 Å as indicated by the fitting curve in **Fig.**  
 194 **4b**<sup>29</sup>. Upon the annealing, diffraction peaks become sharper, evidencing an increase of particle  
 195 size related to the SEM observation in **Fig. 2**. These results of ND measurement are fascinating  
 196 as they clearly demonstrate that the nucleation together with small-size crystals of  $\alpha$ -MnO<sub>2</sub>,  
 197 which cannot be explored by XRD and other methods, have been formed already at room  
 198 temperature. Such a different observation between ND and XRD measurements can be well  
 199 understood because of different scattering properties of neutrons and X-rays, that is, X-rays are  
 200 best suited for materials with shallow depths or thin specimens, whereas neutrons with high  
 201 penetration depth are well applied for bulk samples like  $\alpha$ -MnO<sub>2</sub><sup>30</sup>.



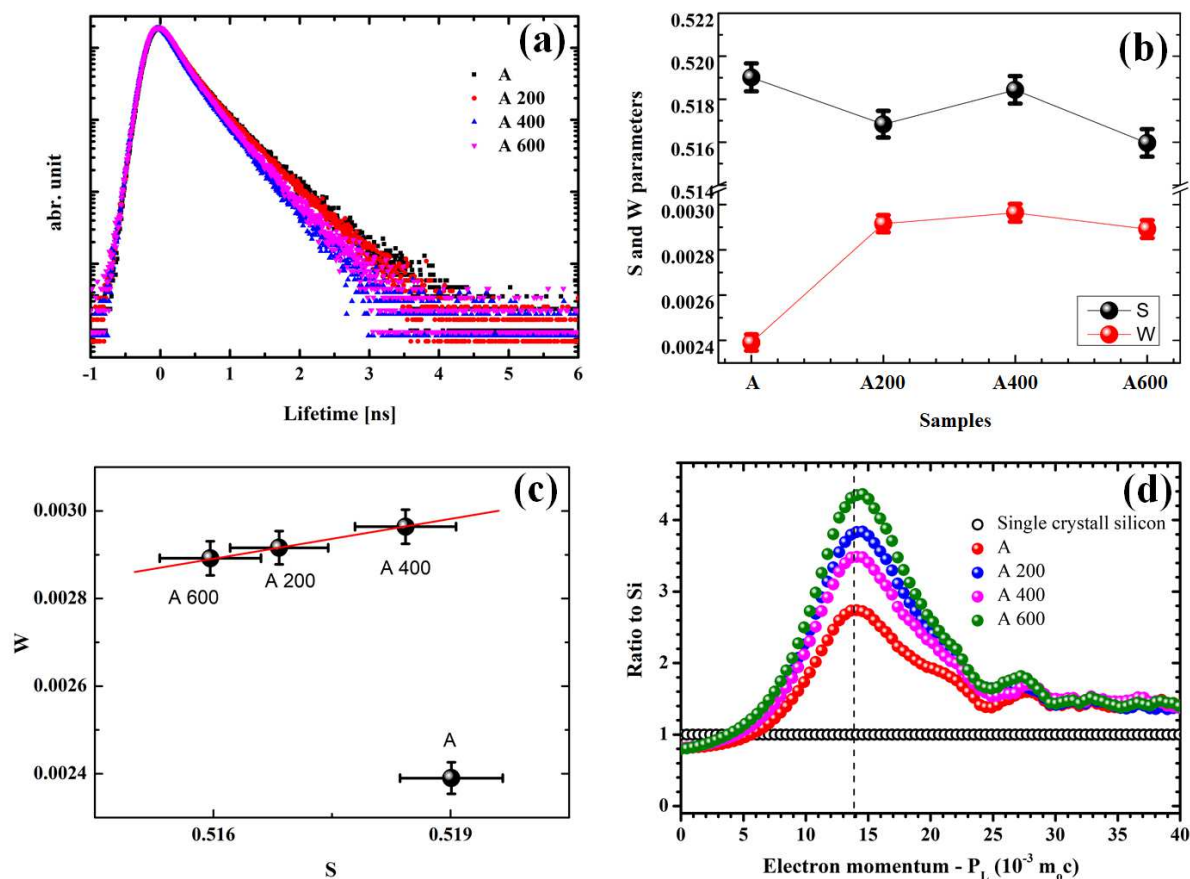
202

203 **Fig. 4. XRD spectra of MnO<sub>x</sub> samples at different temperatures (a) and neutron**  
 204 **diffraction spectra of A and A600 samples (b). Lowest vertical red sticks stand for the**  
 205 **reference diffraction indices associated with XRD and ND peaks.**

206 **PAL analysis.** PAL spectra are presented in **Fig. 5a**, whereas positron lifetime data are given  
 207 in **Supplementary Table 3**. Two positron lifetime components ( $\tau_1$  and  $\tau_2$ ) were found for all  $\alpha$ -  
 208 MnO<sub>2</sub> samples (from A to A600). The lifetimes  $\tau_1$  and  $\tau_2$  are insignificantly changed in the A  
 209 and A200 samples, implying that annealing temperature of 200 °C is insufficient to change the  
 210 basic structure of  $\alpha$ -MnO<sub>2</sub>. However,  $\tau_1$  is strongly decreased from  $\tau_1 = 0.174$  (0.177) ns in A  
 211 (A200) to  $\tau_1 = 0.137$  (0.143) ns in A400 (A600), whereas  $\tau_2$  is slightly reduced from  $\tau_2 = 0.457$   
 212 (0.422) ns in A (A200) to  $\tau_2 = 0.361$  (0.384) ns in A400 (A600). This decrease of  $\tau_1$  and  $\tau_2$  with  
 213 increasing temperature has a close relationship with the reduction of unit cell sizes in  $\alpha$ -MnO<sub>2</sub>  
 214 crystals extracted from XRD spectra (**Supplementary Table 2**). Moreover, the theoretical *ab*  
 215 *initio* calculations for positron lifetimes in different structures of MnO<sub>2</sub> ( $\alpha$ ,  $\beta$ , and  $\gamma$ -MnO<sub>2</sub>) in  
 216 **Supplementary Table 4** show that the calculated positron lifetime in the tunnel [2x2] of  $\alpha$ -  
 217 MnO<sub>2</sub> (0.375 ns) agrees well with the experimental  $\tau_2$  values for the A400 (0.361 ± 0.008 ns)

218 and A600 ( $0.384 \pm 0.009$  ns) samples given in **Supplementary Table 3**. This result strongly  
219 supports our above observation of  $\alpha$ -MnO<sub>2</sub> nanorods above 400 °C (**Figs. 2 and 4**). Moreover,  
220 the calculated positron lifetime in the tunnels [1x1] of  $\alpha$ -MnO<sub>2</sub> (0.154 ns) is slightly higher than  
221 the experimental  $\tau_1$  values of A400 ( $0.137 \pm 0.007$  ns) and A600 ( $0.143 \pm 0.006$  ns) samples.  
222 Such a difference between the simulated and measured  $\tau_1$  values might be due to the existence  
223 of H<sup>+</sup> ions in the tunnel [1x1] of  $\alpha$ -MnO<sub>2</sub> to be discussed hereafter.

224 **DB and EMD measurements.** It is worthwhile to mention that some lattice defects in the forms  
225 of mono-vacancy can contribute to the increase of bulk positron lifetime<sup>31</sup>. Hence, the  
226 contribution of defects to the positron lifetime  $\tau_1$  should be properly considered. This  
227 contribution can be investigated by using DB and EMD measurements. Annihilation parameters  
228 of DB measurement are shown in **Figs. 5b and 5c** and **Supplementary Table 5**. In **Fig. 5b**, the  
229 highest value of S parameter for the A sample suggests the highest concentration of mono-  
230 vacancy defects at low temperature, due to which the values of  $\tau_1$  in the A and A200 samples  
231 are higher than those in the A400 and A600 species. The lowest value of W parameter for the  
232 A sample reveals a different annihilation environment as compared to other samples. This  
233 interesting result reconfirms the existence of organic compound in the A sample predicted  
234 previously by TGA-DSC and FT-IR analyses. Moreover, the correlated plot of S and W  
235 parameters in **Fig. 5c** implies that there should be a similar type of defects existed in the A200,  
236 A400 and A600 samples, whereas the A sample contains a completely different defect. **Fig. 5d**  
237 depicts the ratio curves of EMD in the A – A600 species to that of a pure single-crystal silicon,  
238 which is used for reference. In this figure, all the peaks appear around an electron momentum  
239 of  $14 \times 10^{-3} m_0c$  related to the positron annihilation by 2p electrons of O<sup>32</sup>. These peaks suggest  
240 that some mono-vacancies of Mn were possibly formed in all samples. A shoulder-like peak  
241 appearing in the range of  $15 - 19 \times 10^{-3} m_0c$ , which describes the positron annihilation by 3d  
242 electrons of Mn, is seen for the A sample only. The appearance of this shoulder-like peak  
243 indicates a possible existence of O vacancies in the A sample, similar to that reported for ZnO  
244 materials<sup>33</sup>. Hence, the A sample should contain both vacancies of Mn and O, whereas other  
245 samples mostly contain mono-vacancies of Mn. This result, which has not been reported in any  
246 research so far, indicates that thermal treatment seems to remove mono-vacancies of O from  
247 the samples or increasing temperature would lead to an increase of mono-vacancy concentration  
248 of Mn in the samples.



249  
 250 **Fig. 5. Positron lifetime spectra (a), S and W parameters of Doppler broadening**  
 251 **measurements (b), and correlated plot of S and W parameters (c) for A-A600 samples.**  
 252 **(d) Ratio curves of electron momentum distribution of A-A600 samples to a reference**  
 253 **pure single-crystal silicon.**

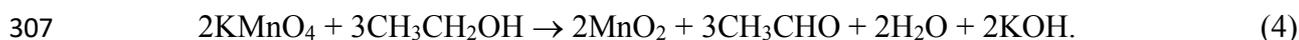
254 **Existence of  $H^+$  ions in  $\alpha$ - $MnO_2$  tunnels.** As discussed in the PAL analysis above, the  
 255 difference between the simulated and measured  $\tau_1$  values might come from the presence of  $H^+$   
 256 ions in the tunnel [1x1] of  $\alpha$ - $MnO_2$ . We, thus, carried out the *ab initio* calculations by placing  
 257  $H^+$  ions with different Mn:H ratios in the tunnel [1x1] of  $\alpha$ - $MnO_2$ . The calculated positron  
 258 lifetimes in this case are found to be shorter than that obtained without  $H^+$  doping as shown in  
 259 **Supplementary Table 6**. By combining the experimental and calculated positron lifetimes in  
 260 **Supplementary Tables 3 and 5**, one could easily find that the experimental lifetimes  $\tau_1$  of  
 261 A400 ( $0.137 \pm 0.007$  ns) and A600 ( $0.143 \pm 0.006$  ns) samples are close to their calculated  
 262 values ( $0.149$  ns and  $0.129$  ns for Mn:H ratios of 0.5 and 1, respectively). This indicates the  
 263 possible existence of  $H^+$  ions in the tunnel [1x1] of  $\alpha$ - $MnO_2$  due to high temperature treatment  
 264 (above  $400$  °C), which cannot be explored by either XRD and/or ND measurements.

265 **B.E.T and B.J.H analyses.** Surface area ( $S_{BET}$ ) and pore diameter of the A, A200, A400, and  
 266 A600 samples are shown in **Supplementary Table 7**. Surface area is decreased from 122 to 28  
 267  $m^2/g$  when temperature is increased from  $100$  °C to  $600$  °C, respectively. Obviously, the A  
 268 sample has the highest  $S_{BET}$  value because of its nucleation and small-size crystals at  $100$  °C.  
 269 There is a slight decrease of  $S_{BET}$  due to aggregation when temperature is increased from  $100$   
 270 °C to  $200$  °C. With increasing temperature to  $400$  °C,  $S_{BET}$  is dropped by a factor of 2 (to  
 271  $60$   $m^2/g$ ). Finally,  $S_{BET}$  is decreased dramatically when temperature reaches  $600$  °C at which the  $\alpha$ -  
 272  $MnO_2$  nanorod structure is completely developed (**Fig. 2**). In addition, B.J.H analysis also  
 273 reveals the mesoporous structure of all studied samples because their pore sizes determined  
 274 from this B.J.H are higher than  $2$  nm but less than  $50$  nm<sup>34,35</sup>.

275 The present study reports, for the first time, a novel evolution of  $\alpha$ -MnO<sub>2</sub> nanomaterial  
276 synthesized using a facile chemical method at different temperatures from 100 °C to 800 °C.  
277 Crystallization pathways, morphologies and structural defects of the synthesized materials are  
278 studied in detail by combining the physical, chemical, and nuclear analytical methods together  
279 with theoretical calculations. Results obtained show that the nucleation of  $\alpha$ -MnO<sub>2</sub> can be  
280 formed even at room temperature. This surprising result, which cannot be determined by using  
281 the conventional XRD method, is confirmed by the neutron diffraction and positron annihilation  
282 lifetime measurements combined with the calculated positron lifetime. The evolution of  
283 crystalline structure with temperature can be seen by using TGA-DSC analysis and SEM  
284 images, in which the  $\alpha$ -MnO<sub>2</sub> nucleation and small-size crystals are grown to nanowires as  
285 temperature is increased from 100 °C to 400 °C, prior to forming nanorods above 500 °C. This  
286 growth directly affects the material's surface area and morphology as can be seen in B.E.T and  
287 B.J.H analyses. Moreover, by comparing experimental positron lifetimes with simulated results,  
288 we have found an possible existence of H<sup>+</sup> ions in the tunnel [1x1] of  $\alpha$ -MnO<sub>2</sub> with the ratio of  
289 Mn:H ranging from 0.5 to 1. This is the first experimental evidence supported by theoretical  
290 calculations showing such an existence of H<sup>+</sup> ions in the tunnel [1x1] of  $\alpha$ -MnO<sub>2</sub>. Another  
291 notable result obtained within the present study is that organic molecules not only play as  
292 reducing agents in the oxidation-reduction reaction between KMnO<sub>4</sub> and C<sub>2</sub>H<sub>5</sub>OH but also act  
293 as templates, which gradually form nanorods from nucleation. This finding is consistent with  
294 the FT-IR analysis and positron lifetime measurements. The present study is, therefore, of  
295 particular important as it provides detailed and profound views on the crystallization pathways,  
296 morphologies and structures of nanomaterials as  $\alpha$ -MnO<sub>2</sub>, which are fundamental information  
297 for their applications in diverse areas.

## 298 **Methods**

299 **Materials synthesis.** MnO<sub>2</sub> nanomaterial was synthesized using a facile chemical method  
300 based on the oxidation-reduction reaction between saturated KMnO<sub>4</sub> solution and C<sub>2</sub>H<sub>5</sub>OH  
301 alcohol as **Eq. 4**. The synthesis procedure is illustrated in **Supplementary Fig. 2**. Herein, 30  
302 grams of KMnO<sub>4</sub> was dissolved in 500 mL of deionized water to obtain the saturated KMnO<sub>4</sub>  
303 solution. This solution was then gradually added into 250 mL of C<sub>2</sub>H<sub>5</sub>OH alcohol with a  
304 dropping speed of 2 mL/min. The reaction was performed within 24 h with 1200 revolutions  
305 per minute (rpm). After that, the obtained solid powder was washed with distilled water, prior  
306 to being stored in the oven at 100 °C.



308 The obtained MnO<sub>2</sub> samples were divided into different portions based on their annealed  
309 temperatures. The portions abbreviated by A200 to A800 correspond to those annealed by  
310 temperatures of 200 °C to 800 °C, respectively. The sample denoted by A is the original sample  
311 synthesized at room temperature and then annealed to 100 °C to remove the absorbed water.

312 **Characterizations.** Powder X-ray diffraction (PXRD) measurements were performed using a  
313 X-ray diffractometer D8 Advance Eco (Bruker) equipped with a Cu-K $\alpha$  radiation source ( $\lambda =$   
314 1.54056 Å). Scanning electron microscopy (SEM) was carried out by a S-4800, Hitachi, Japan.  
315 Temperature programmed reduction (TPR) experiments were operated using an AMI-902  
316 (Altamira) analyzer equipped with a TCD detector. In the TPR experiment, all samples were  
317 pre-treated under Ar at 400 °C for 30 minutes and cooled down to 50 °C under Ar atmosphere.  
318 The reduction step was carried out from 100 °C up to 500 °C under 1 % H<sub>2</sub> in Ar with a heating  
319 rate of 5 K.min<sup>-1</sup>. A TRISTAR 3020 Micrometrics apparatus and a ASTM D 3663 procedure  
320 were used to evaluate the surface areas (SA) and pore volumes (PV) of all samples. Prior to the

321 measurement, the samples were degassed at 260 °C for 4 h in N<sub>2</sub> using SmartPrep 065 degassing  
322 unit.

323 **Neutron diffraction (ND).** ND experiments were carried out at the IBR-2 high flux pulsed  
324 reactor at Joint Institute for Nuclear Research (Dubna, Russia). In this experiment, a DN-6  
325 diffractometer<sup>36</sup> was used to measure two powder samples of  $\alpha$ -MnO<sub>2</sub> (A and A600 samples).  
326 The measurements were performed at a scattering angle of 90° with a resolution  $\Delta d/d = 0.015$   
327 at the ambient temperature. The experimental data were analyzed by Rietveld method using the  
328 FullProf program<sup>37</sup>.

329 **Positron annihilation lifetime (PAL).** A conventional fast-fast coincident analog system  
330 (Ortec Co. Ltd) and a digital positron lifetime spectrometer APV8702 (TechnoAP Co. Ltd.)  
331 were used to measure the positron lifetimes. The former consists of two plastic scintillation  
332 detectors (Ortec)<sup>38</sup>, whereas the latter contains two photomultipliers H3378-50 coupled with  
333 BaF<sub>2</sub> scintillators<sup>39</sup>. The time resolution of spectrometers at the full-width half maximum is  
334 about 180 – 200 ps. A radioactive isotope <sup>22</sup>Na was used as the positron source encapsulated  
335 into a titanium foil of 7  $\mu$ m thickness with an activity of about 27  $\mu$ Ci. Two identically prepared  
336 samples were placed on both sides of the positron source in order to detect the coincident  
337 events<sup>39</sup>.

338 **Doppler broadening (DB) of positron annihilation radiation and electron momentum**  
339 **distribution (EMD).** A HPGe detector (ORTEC GEM25P4-20) with an energy resolution of  
340 1.20 keV at the 511 keV energy peak (annihilation peak) was used to obtain the DB spectra. In  
341 this DB measurement, two parameters S and W are often used to describe the quanta resulting  
342 from positron annihilation with valence and core electrons, respectively<sup>40</sup>. Here, S is determined  
343 by the ratio of the area under the center of annihilation peak to the total peak area, whereas W  
344 is calculated based on the ratio of the areas under the wing regions on both sides of annihilation  
345 peak to the total peak area<sup>33</sup>. The longitudinal electron momentum can be converted from DB  
346 spectra. It is well-known that the electron momentum has a close relation with positron  
347 annihilation sites, which can be used to determine the types of defect and information about  
348 surrounding atoms. In this analysis, the EMD is obtained based on the ratio of the normalized  
349 spectra of the samples to the normalized spectrum of a standard single-crystal silicon used for  
350 reference<sup>33,38</sup>.

351 **Ab initio calculation of positron lifetime.** Numerical calculations for positron lifetime in  
352 MnO<sub>2</sub> phases were carried out using PAW formalism implemented in ABINIT v 8.4.4<sup>41</sup>. PAW  
353 potentials for Mn, O, K, and H were taken from the pseudopotential ABINIT JTHv1.1  
354 repository<sup>42,43</sup>. A K-point space was sampled by a 6×6×6 Monkhorst–Pack set, which  
355 corresponds to 12 K-points<sup>41</sup>. The bulk positron-lifetime computations were performed on 96  
356 atoms of Mn and O supercell constructed on the basis of unit cell<sup>44,45</sup>. The calculations with  
357 filled tunnels by hydrogen atoms with different ratios of Mn:H were carried out as given in  
358 **Supplementary Table 7**. For practical calculations, an enhancement factor of the Boronski-  
359 Nieminen in the limit of RPA parametrization was used<sup>46</sup>.

360

361

## 362 References

- 363 1. Fernandes, J.B., Desai, B.D. & Dalal, V.N.K. Manganese dioxide-a review of a battery  
364 chemical part I. Chemical syntheses and x-ray diffraction studies of manganese  
365 dioxides. *J. Power Sources* **15**, 209-237 (1985).

- 366 2. Miao, L., Wang, J. & Zhang, P. Review on manganese dioxide for catalytic oxidation  
367 of airborne formaldehyde. *Appl. Surf. Sci.* **466**, 441-453 (2019).
- 368 3. Aronson, B.J., Blanford, C.F. & Stein, A. Synthesis, characterization, and ion-exchange  
369 properties of zinc and magnesium manganese oxides confined within MCM-41  
370 channels. *J. Phys. Chem. B* **104**, 449-459 (2000).
- 371 4. Brock, S.L., *et al.* A review of porous manganese oxide materials. *Chem. Mater.* **10**,  
372 2619-2628 (1998).
- 373 5. Toroker, M.C. & Carter, E.A. Transition metal oxide alloys as potential solar energy  
374 conversion materials. *J. Mater. Chem. A* **1**, 2474-2484 (2013).
- 375 6. Post, J.E. Manganese oxide minerals: Crystal structures and economic and  
376 environmental significance. *Proc. Natl. Acad. Sci. USA* **96**, 3447-3454 (1999).
- 377 7. Song, H., *et al.* A hollow urchin-like  $\alpha$ -MnO<sub>2</sub> as an electrochemical sensor for hydrogen  
378 peroxide and dopamine with high selectivity and sensitivity. *Microchim. Acta.* **186**, 210  
379 (2019).
- 380 8. Saputra, E., *et al.*  $\alpha$ -MnO<sub>2</sub> activation of peroxydisulfate for catalytic phenol  
381 degradation in aqueous solutions. *Catal. Commun.* **26**, 144-148 (2012).
- 382 9. Li, L., Nan, C., Lu, J., Peng, Q. & Li, Y.  $\alpha$ -MnO<sub>2</sub> nanotubes: high surface area and  
383 enhanced lithium battery properties. *Chem. Comm.* **48**, 6945-6947 (2012).
- 384 10. Zhang, R., *et al.*  $\alpha$ -MnO<sub>2</sub> as a cathode material for rechargeable Mg batteries.  
385 *Electrochem. Commun.* **23**, 110-113 (2012).
- 386 11. Shen, Y.F., *et al.* Manganese oxide octahedral molecular sieves: preparation,  
387 characterization, and applications. *Science* **260**, 511-515 (1993).
- 388 12. Scrivens, G., Ticehurst, M. & Swanson, J.T. in *Accelerated Predictive Stability* (eds.  
389 Qiu, F. & Scrivens, G.) 175-206 (Academic Press, Boston, 2018).
- 390 13. Norton, J.T. Uses and limitations of X-ray diffraction methods. *J. Appl. Phys.* **8**, 307-  
391 312 (1937).
- 392 14. Gabbott, P. in *Principles and Applications of Thermal Analysis* (ed. Gabbott, P.) 1-50  
393 (Blackwell Publishing Ltd, 2008).
- 394 15. Wagner, M. in *Thermal Analysis in Practice* (ed. Wagner, M.) 10-15 (Hanser, 2018).
- 395 16. Said, M.I. & Harbrecht, B. Controlled synthesis of Mn<sub>5</sub>O<sub>8</sub> and  $\beta$ -MnO<sub>2</sub> nanorods via  
396 thermal decomposition of  $\gamma$ -MnOOH precursor: Characterization and magnetic  
397 properties of Mn<sub>5</sub>O<sub>8</sub>. *J. Alloys Compd.* **710**, 635-643 (2017).
- 398 17. Kim, S.H., Kim, S.J. & Oh, S.M. Preparation of layered MnO<sub>2</sub> via thermal  
399 decomposition of KMnO<sub>4</sub> and its electrochemical characterizations. *Chem. Mater.* **11**,  
400 557-563 (1999).
- 401 18. Tang, W., *et al.* Sol-gel process for the synthesis of ultrafine MnO<sub>2</sub> nanowires and  
402 nanorods. *Mater. Lett.* **132**, 317-321 (2014).
- 403 19. Ahn, M.-S., Ahmad, R., Yoo, J.-Y. & Hahn, Y.-B. Synthesis of manganese oxide  
404 nanorods and its application for potassium ion sensing in water. *J. Colloid Interface Sci*  
405 **516**, 364-370 (2018).
- 406 20. Su, D., Ahn, H.-J. & Wang, G. Hydrothermal synthesis of  $\alpha$ -MnO<sub>2</sub> and  $\beta$ -MnO<sub>2</sub>  
407 nanorods as high capacity cathode materials for sodium ion batteries. *J. Mater. Chem.*  
408 *A* **1**, 4845-4850 (2013).
- 409 21. Tseng, L.-T., *et al.* Magnetic properties in  $\alpha$ -MnO<sub>2</sub> doped with alkaline elements. *Sci.*  
410 *Rep.* **5**, 9094 (2015).
- 411 22. Li, W., *et al.* Performance modulation of  $\alpha$ -MnO<sub>2</sub> nanowires by crystal facet  
412 engineering. *Sci. Rep.* **5**, 8987 (2015).
- 413 23. Varshney, G., *et al.* Nanoscale TiO<sub>2</sub> films and their application in remediation of organic  
414 pollutants. *Coord. Chem. Rev.* **306**, 43-64 (2016).
- 415 24. Deepak, P., *et al.* in *Green Synthesis, Characterization and Applications of*  
416 *Nanoparticles* (eds. Shukla, A.K. & Irvani, S.) 369-387 (Elsevier, 2019).

- 417 25. Subramanian, V., Zhu, H. & Wei, B. Alcohol-assisted room temperature synthesis of  
418 different nanostructured manganese oxides and their pseudocapacitance properties in  
419 neutral electrolyte. *Chem. Phys. Lett.* **453**, 242-249 (2008).
- 420 26. Chodankar, N.R., Gund, G.S., Dubal, D.P. & Lokhande, C.D. Alcohol mediated growth  
421 of  $\alpha$ -MnO<sub>2</sub> thin films from KMnO<sub>4</sub> precursor for high performance supercapacitors.  
422 *RSC Adv.* **4**, 61503-61513 (2014).
- 423 27. Chen, B.-R., *et al.* Understanding crystallization pathways leading to manganese oxide  
424 polymorph formation. *Nat. Commun.* **9**, 2553 (2018).
- 425 28. Lê, P.N., *et al.* Influence of Mn and Fe addition on the NO<sub>x</sub> storage–reduction properties  
426 and SO<sub>2</sub> poisoning of a Pt/Ba/Al<sub>2</sub>O<sub>3</sub> model catalyst. *Top. cattal.* **52**, 1771 (2009).
- 427 29. Johnson, C.S., *et al.* Structural and electrochemical studies of  $\alpha$ -manganese dioxide ( $\alpha$ -  
428 MnO<sub>2</sub>). *J. Power Sources* **68**, 570-577 (1997).
- 429 30. Bacon, G.E. in *Neutron diffraction. Third Edition* (Oxford University Press, 1975).
- 430 31. Šedivý, L., Čížek, J., Belas, E., Grill, R. & Melikhova, O. Positron annihilation  
431 spectroscopy of vacancy-related defects in CdTe:Cl and CdZnTe:Ge at different  
432 stoichiometry deviations. *Sci. Rep.* **6**, 20641 (2016).
- 433 32. Huang, Y.Y., *et al.* Positron annihilation studies on La<sub>1-x</sub>Sr<sub>x</sub>MnO<sub>3</sub> manganites. *Defect*  
434 *Diffus. Forum* **373**, 201-204 (2017).
- 435 33. Pasang, T., *et al.* Single and couple doping ZnO nanocrystals characterized by positron  
436 techniques. *Mater. Res. Express* **2**, 045502 (2015).
- 437 34. Li, W., Liu, J. & Zhao, D. Mesoporous materials for energy conversion and storage  
438 devices. *Nat. Rev. Mater.* **1**, 16023 (2016).
- 439 35. Sing, K.S.W. in *Studies in Surface Science and Catalysis*, Vol. 62 (eds. Rodriguez-  
440 Reinoso, F., Rouquerol, J., Sing, K.S.W. & Unger, K.K.) 1-9 (Elsevier, 1991).
- 441 36. Kozlenko, D., Kichanov, S., Lukin, E. & Savenko, B. The DN-6 neutron diffractometer  
442 for high-pressure research at half a megabar scale. *Cryst.* **8**, 331 (2018).
- 443 37. Rodríguez-Carvajal, J. Recent advances in magnetic structure determination by neutron  
444 powder diffraction. *Physica B Condens. Matter.* **192**, 55-69 (1993).
- 445 38. Pham, A.T.T., *et al.* Multi-scale defects in ZnO thermoelectric ceramic materials co-  
446 doped with In and Ga. *Ceram. Int.* **46**, 10748-10758 (2020).
- 447 39. Horodek, P. Positron annihilation studies of irradiation-induced defects with swift  
448 heavy ions in gold. *Vacuum* **164**, 421-427 (2019).
- 449 40. Parmar, N.S. & Lynn, K.G. Sodium doping in ZnO crystals. *Appl. Phys. Lett* **106**,  
450 022101 (2015).
- 451 41. Dryzek, J. & Siemek, K. Defects and their range in pure bismuth irradiated with swift  
452 Xe ions studied by positron annihilation techniques. *Appl. Phys. A* **125**, 85 (2019).
- 453 42. Wiktor, J., Jomard, G. & Torrent, M. Two-component density functional theory within  
454 the projector augmented-wave approach: Accurate and self-consistent computations of  
455 positron lifetimes and momentum distributions. *Phys. Rev. B* **92**, 125113 (2015).
- 456 43. Torrent, M., Jollet, F., Bottin, F., Zérah, G. & Gonze, X. Implementation of the projector  
457 augmented-wave method in the ABINIT code: Application to the study of iron under  
458 pressure. *Comput. Mater. Sci.* **42**, 337-351 (2008).
- 459 44. Kondrashev, Y.D. & Zaslavskii, A.I. The structure of the modifications of  
460 manganese(IV) oxide. *Izv. Akad. Nauk SSSr, Ser. Fiz.* **15**, 179 - 186 (1951).
- 461 45. Sun, M., *et al.* Manganese oxides with different crystalline structures: Facile  
462 hydrothermal synthesis and catalytic activities. *Mater. Lett.* **86**, 18-20 (2012).
- 463 46. Boroński, E. & Nieminen, R.M. Electron-positron density-functional theory. *Phys. Rev.*  
464 *B* **34**, 3820-3831 (1986).

465

466

467 **Acknowledgements**

468 This research is funded by Vietnam National Foundation for Science and Technology  
469 Development (NAFOSTED) under Grant number 103.02-2018.368. L. Anh Tuyen  
470 acknowledges the annual research assignments by the Vietnam Atomic Energy Institute.

471

472

473 **Author contributions**

474 Van-Phuc Dinh, L. Anh Tuyen, and N. Quang Hung proposed the research. Van-Phuc Dinh,  
475 Ngoc-Chung Le and L. Anh Tuyen designed the experiments. Van-Phuc Dinh, L. Anh Tuyen,  
476 Le-Phuc Nguyen, P. T. Phuc, Tran Duy Tap, Thien-Hoang Ho, and L. T. Son performed the  
477 material synthesis, characterization, and positron annihilation measurements. Krzysztof Siemek  
478 carried out the *ab initio* calculations for the positron lifetimes. Van-Phuc Dinh, Le-Phuc  
479 Nguyen and Thuy Ngoc Luong measured the TPR-H<sub>2</sub> spectra and analyzed the data. D. P.  
480 Kozlenko, L. H. Khiem, and N. D. Toan performed the neutron diffraction measurements and  
481 analyzed the data. N. V. Tiep, H. A. T. Kiet, T. D. Xuan and Ngoc-Tuan Nguyen discussed and  
482 analyzed data. Van-Phuc Dinh, L. Anh Tuyen and N. Quang Hung wrote the original draft. All  
483 authors discussed the results and commented on the manuscript.

484 **Additional information**

485 Supplementary information is available online. Reprints and permissions information is  
486 available online at [www.nature.com/reprints](http://www.nature.com/reprints). Correspondence and requests for materials should  
487 be addressed to Van-Phuc Dinh or L. Anh Tuyen or N. Quang Hung.

488 **Competing interests**

489 The authors declare no competing financial interests.

490

491 SUPPLEMENTARY INFORMATION

492  
493 **Crystallization pathways, morphologies and structural defects of  $\alpha$ -MnO<sub>2</sub>**  
494 **nanomaterial synthesized under annealed temperatures**

495 Van-Phuc Dinh<sup>1,2,\*</sup>, L. Anh Tuyen<sup>3,4,\*</sup>, K. Siemek<sup>4,5</sup>, D. P. Kozlenko<sup>6</sup>, L. Hong Khiem<sup>7,8</sup>, N.  
496 T. Dang<sup>9,2</sup>, N. Van Tiep<sup>7,10</sup>, Le-Phuc Nguyen<sup>11</sup>, Tran Duy Tap<sup>12,13</sup>, P. Trong Phuc<sup>3</sup>, L. Thai  
497 Son<sup>3</sup>, H. A. Tuan Kiet<sup>9,14</sup>, D. Thanh Khan<sup>15</sup>, Thuy Ngoc Luong<sup>11</sup>, Ngoc-Chung Le<sup>16</sup>, Ngoc-  
498 Tuan Nguyen<sup>17</sup>, Thien-Hoang Ho<sup>18</sup>, T. Dong Xuan<sup>1,2</sup>, N. Quang Hung<sup>1,2,\*</sup>  
499

500 <sup>1</sup>*Institute of Fundamental and Applied Sciences, Duy Tan University, Ho Chi Minh City*  
501 *700000, Viet Nam*

502 <sup>2</sup>*Faculty of Natural Sciences, Duy Tan University, Da Nang City 550000, Viet Nam*

503 <sup>3</sup>*Center Nuclear Technologies, Vietnam Atomic Energy Institute, Ho Chi Minh City 700000,*  
504 *Viet Nam*

505 <sup>4</sup>*Dzhelepov Laboratory of Nuclear Problems, JINR, 141980 Dubna, Moscow Reg., Russia*

506 <sup>5</sup>*Institute of Nuclear Physics, Polish Academy of Sciences, PL-31342 Krakow, Poland*

507 <sup>6</sup>*Frank Laboratory of Neutron Physics, JINR, 141980 Dubna, Moscow Reg., Russia*

508 <sup>7</sup>*Institute of Physics, Viet Nam Academy of Science and Technology, 10 Dao Tan, Ba Dinh, Ha*  
509 *Noi City 100000, Viet Nam*

510 <sup>8</sup>*Graduate University of Science and Technology, Vietnam Academy of Science and*  
511 *Technology, 18 Hoang Quoc Viet, Ha Noi City 100000, Viet Nam*

512 <sup>9</sup>*Institute of Research and Development, Duy Tan University, Da Nang City 550000, Viet Nam*

513 <sup>10</sup>*Flerov Laboratory of Nuclear Reactions, JINR, 141980 Dubna, Moscow Reg., Russia*

514 <sup>11</sup>*Vietnam Petroleum Institute, Ho Chi Minh City 700000, Viet Nam*

515 <sup>12</sup>*Faculty of Materials Science and Technology, University of Science, VNU–HCMC, 227*  
516 *Nguyen Van Cu, District 5, Ho Chi Minh City 700000, Viet Nam*

517 <sup>13</sup>*Vietnam National University Ho Chi Minh City, Ho Chi Minh City 700000, Viet Nam*

518 <sup>14</sup>*Graduate School of Education, University of Pennsylvania, Philadelphia, Pennsylvania*  
519 *19104, USA*

520 <sup>15</sup>*University of Science and Education, The University of Da Nang, Da Nang City 550000, Viet*  
521 *Nam*

522 <sup>16</sup>*DaLat University, Dalat University, 01 Phu Dong Thien Vuong, Da Lat City 670000, Viet*  
523 *Nam*

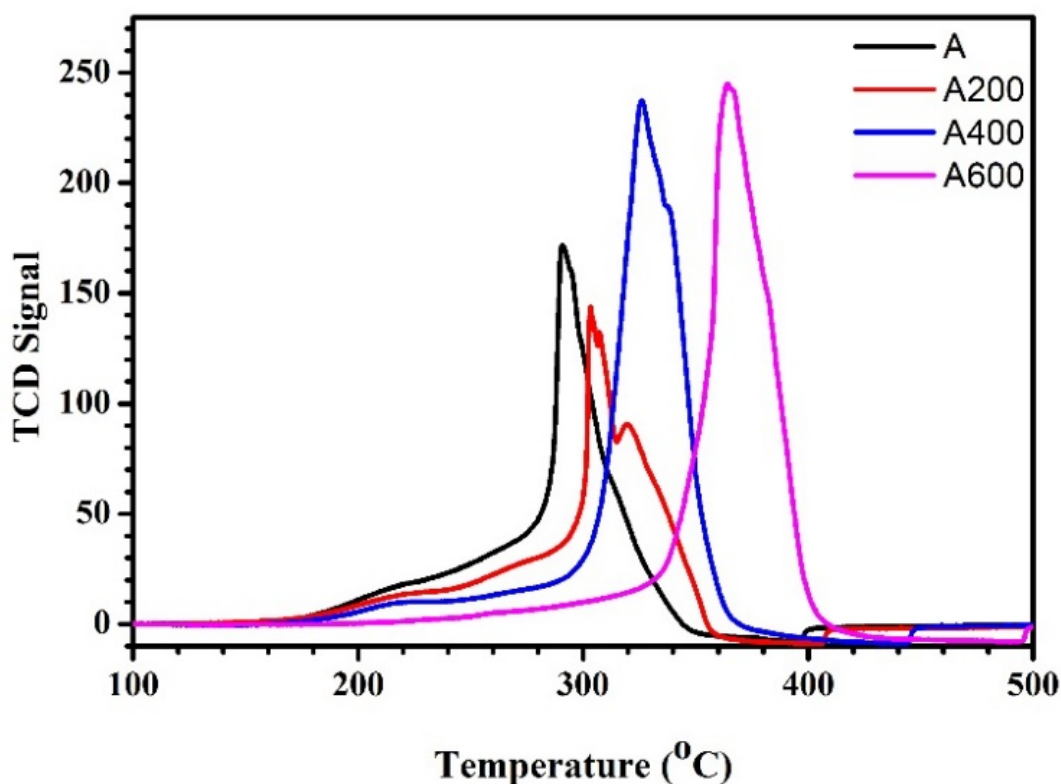
524 <sup>17</sup>*Dalat Nuclear Research Institute, 01 Nguyen Tu Luc, Da Lat City 670000, Viet Nam*

525 <sup>18</sup>*Dong Nai University, Le Quy Don Street, Bien Hoa City, Dong Nai 810000, Viet Nam*

526  
527 *Corresponding author: [dinhvanphuc@duytan.edu.vn](mailto:dinhvanphuc@duytan.edu.vn); [tuyenhuuanh@gmail.com](mailto:tuyenhuuanh@gmail.com);*  
528 *[nguyenquanghung5@duytan.edu.vn](mailto:nguyenquanghung5@duytan.edu.vn)*

530

531

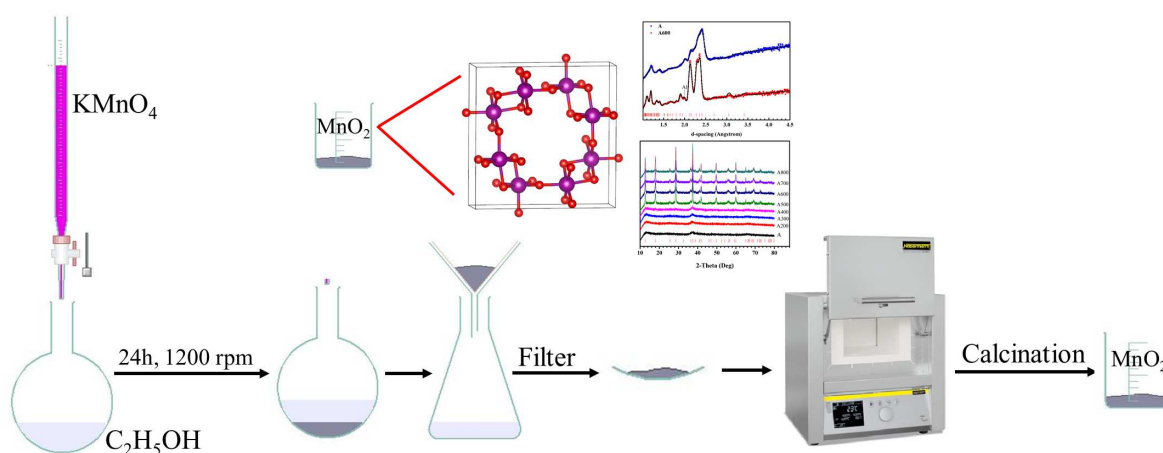


532

Supplementary Figure 1. TPR-H<sub>2</sub> plots for different MnO<sub>x</sub> samples

533

534



535

Supplementary Figure 2. Illustration of synthesis procedures of MnO<sub>2</sub> via a facile chemical method

536

537

Supplementary Table 1. H<sub>2</sub> uptake and experimental formula of MnO<sub>x</sub>

538

Sample	TPR peak position (°C)			H <sub>2</sub> uptake (μmol.g <sup>-1</sup> )	x	Experimental Formula
	1	2	3			
A	256	293	303	11038	1.952	MnO <sub>1.952</sub>
A200	280	305	321	11101	1.959	MnO <sub>1.959</sub>
A400	302	326	338	11507	2.001	MnO <sub>2.001</sub>
A600	357	364	378	11560	2.005	MnO <sub>2.005</sub>

539

540 **Supplementary Table 2. Unit cell sizes of A400-A800 samples calculated from XRD**  
 541 **patterns**

Sample	Unit cell size (XRD)		
	a = b (Å)	c (Å)	Cell volume (Å <sup>3</sup> )
A400	9.78450	2.88550	276.2476
A500	9.77659	2.87625	274.9167
A600	9.77128	2.87576	274.5712
A700	9.76160	2.87708	274.1536
A800	9.77871	2.87594	275.0068

542  
 543 **Supplementary Table 3. Experimental positron lifetimes  $\tau$  and their intensities I**  
 544 **obtained for all studied samples**

Sample	$\tau_1$ (ns)	$\tau_2$ (ns)	I <sub>1</sub> (%)	I <sub>2</sub> (%)
A	0.174 ± 0.006	0.457 ± 0.009	45.70 ± 1.22	54.30 ± 1.41
A200	0.177 ± 0.005	0.442 ± 0.010	46.13 ± 1.37	53.87 ± 1.83
A400	0.137 ± 0.007	0.361 ± 0.008	36.69 ± 0.97	63.31 ± 1.92
A600	0.143 ± 0.006	0.384 ± 0.009	40.54 ± 1.02	59.46 ± 1.84

545  
 546 **Supplementary Table 4. Calculated positron lifetimes for different tunnel structures of**  
 547 **MnO<sub>2</sub>**

MnO <sub>2</sub> structure	Positron lifetime (ns)
$\beta$ -MnO <sub>2</sub> for tunnel [1x1]	0.152
$\gamma$ -MnO <sub>2</sub> for tunnel [1x2]	0.190
$\alpha$ -MnO <sub>2</sub> for tunnel [1x1]	0.154
$\alpha$ -MnO <sub>2</sub> for tunnel [2x2]	0.375

548  
 549 **Supplementary Table 5. Annihilation parameters W and S of Doppler broadening**  
 550 **measurements**

Sample	S	W
A	0.51901 ± 0.00065	0.002390 ± 0.000036
A200	0.51683 ± 0.00062	0.002916 ± 0.000038
A400	0.51843 ± 0.00064	0.002964 ± 0.000039
A600	0.51596 ± 0.00064	0.002892 ± 0.000039

552

553

554

**Supplementary Table 6. Calculated positron lifetimes in the tunnel [1x1] of  $\alpha$ -MnO<sub>2</sub> doped with H<sup>+</sup> ions using different Mn:H ratios**

<b>Mn:H ratio</b>	<b>Positron lifetime (ns)</b>
0.5	149
1.0	129
1.5	119
2.0	112

555

556

**Supplementary Table 7. B.E.T surface area and B.J.H pore diameter**

<b>Sample</b>	<b>B.E.T surface area (m<sup>2</sup>/g)</b>	<b>Pore size (nm)</b>
A	122	10.9 – 11.7
A200	109	11.5 – 12.1
A400	60	10.6 – 13.9
A600	28	7.8 – 10.1

557

# Figures

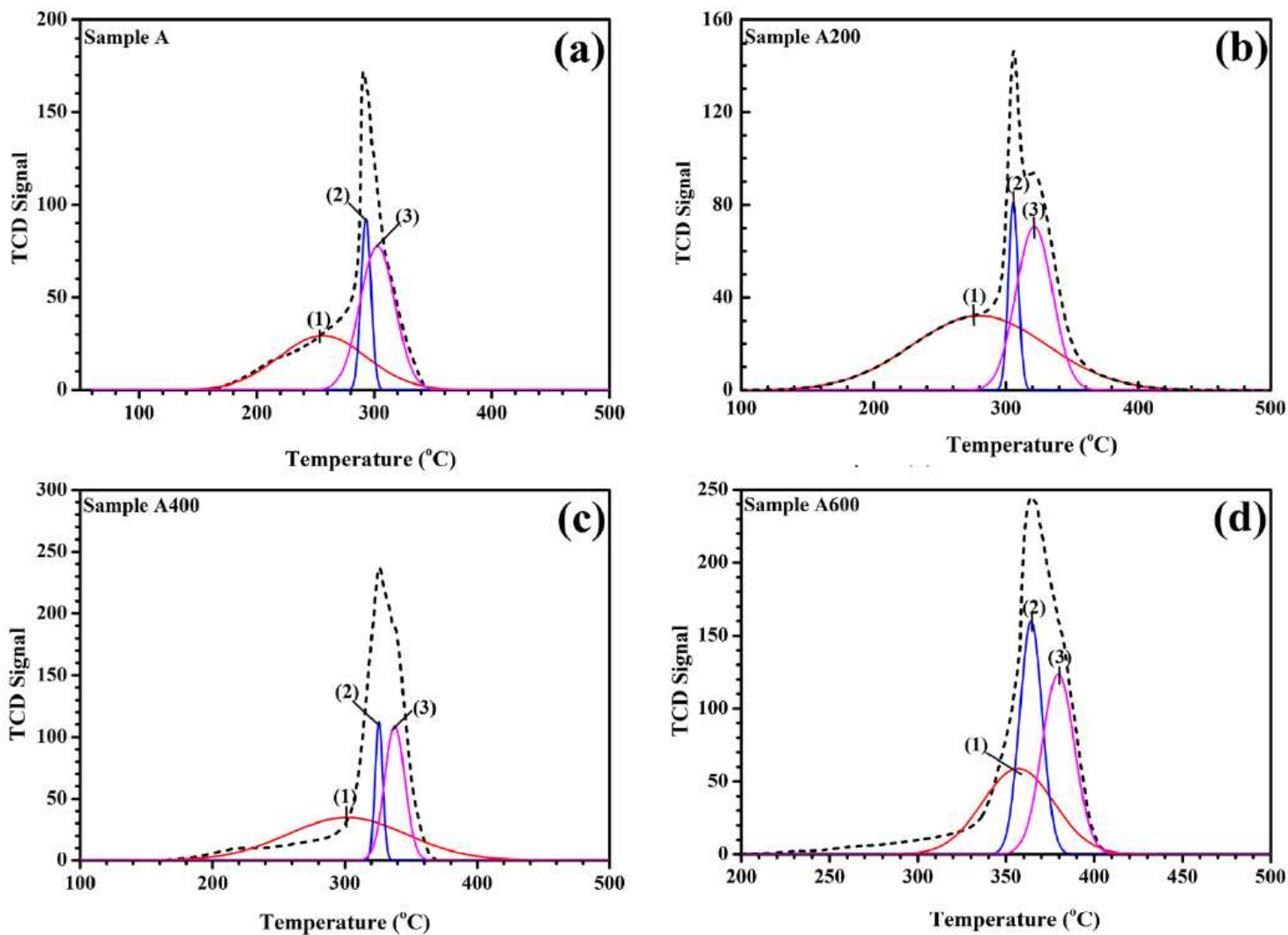
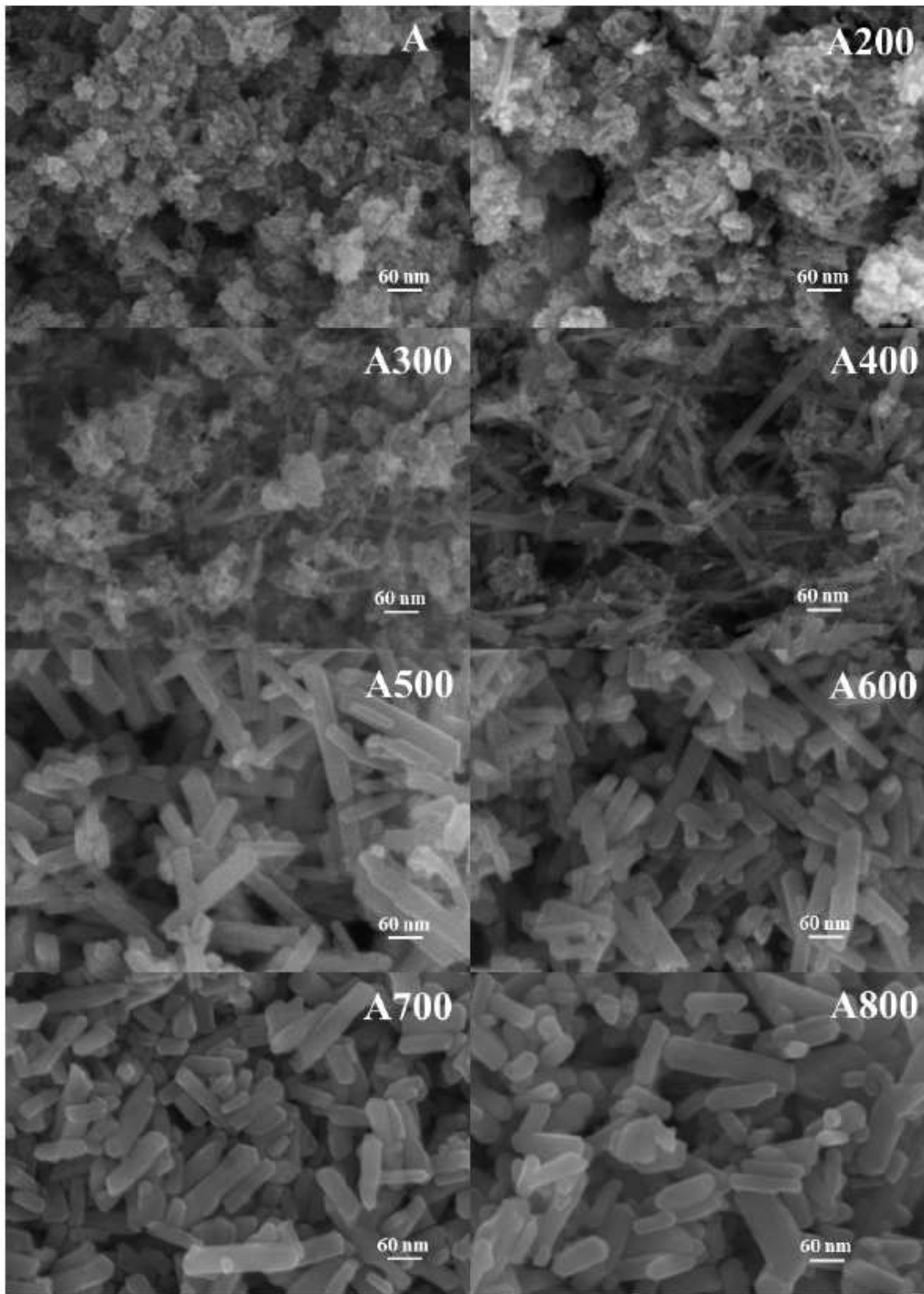


Figure 1

TPR-H<sub>2</sub> profiles of different MnO<sub>x</sub> samples according to three stages: (1) MnO<sub>2</sub> → Mn<sub>2</sub>O<sub>3</sub>, (2) Mn<sub>2</sub>O<sub>3</sub> → Mn<sub>3</sub>O<sub>4</sub>, and (3) Mn<sub>3</sub>O<sub>4</sub> → MnO.



**Figure 2**

SEM images of all studied samples at different annealed temperatures.

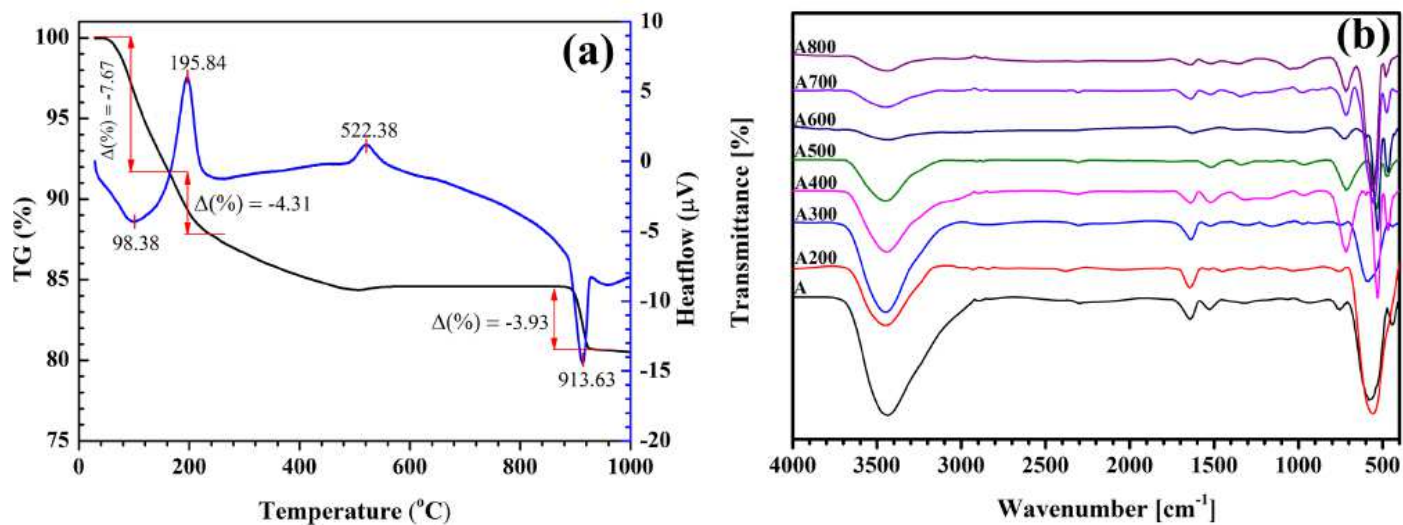


Figure 3

TGA-DSC of MnO<sub>2</sub> powder (A sample) in air (a) and FT-IR spectra of MnO<sub>2</sub> samples (b)

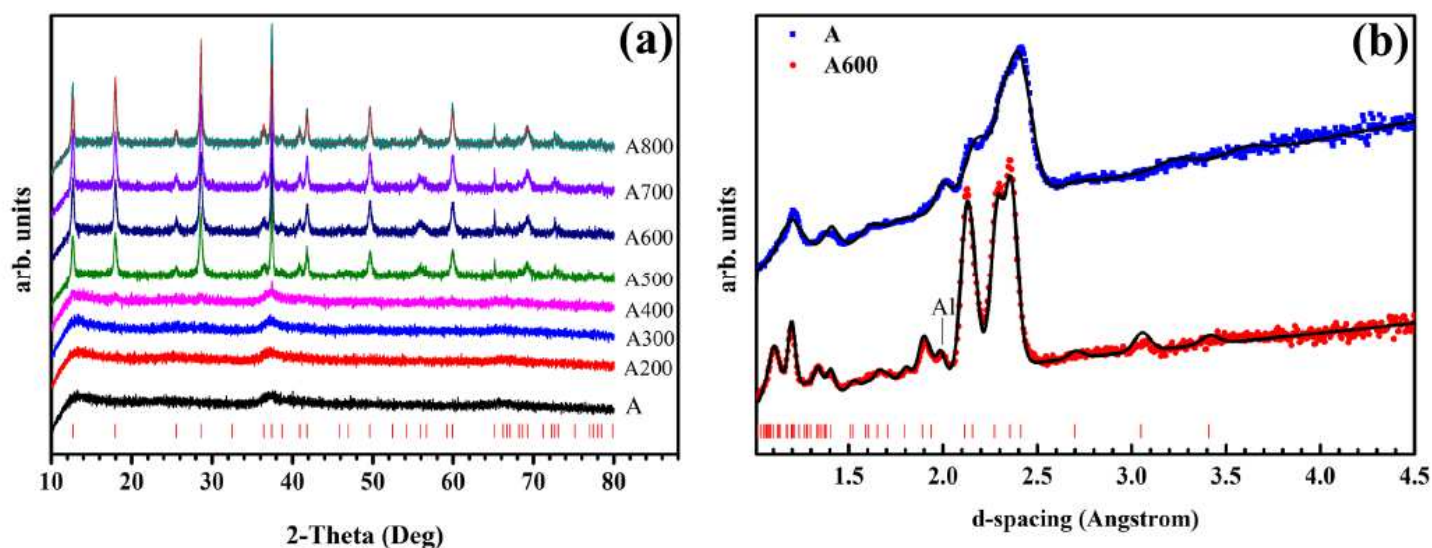
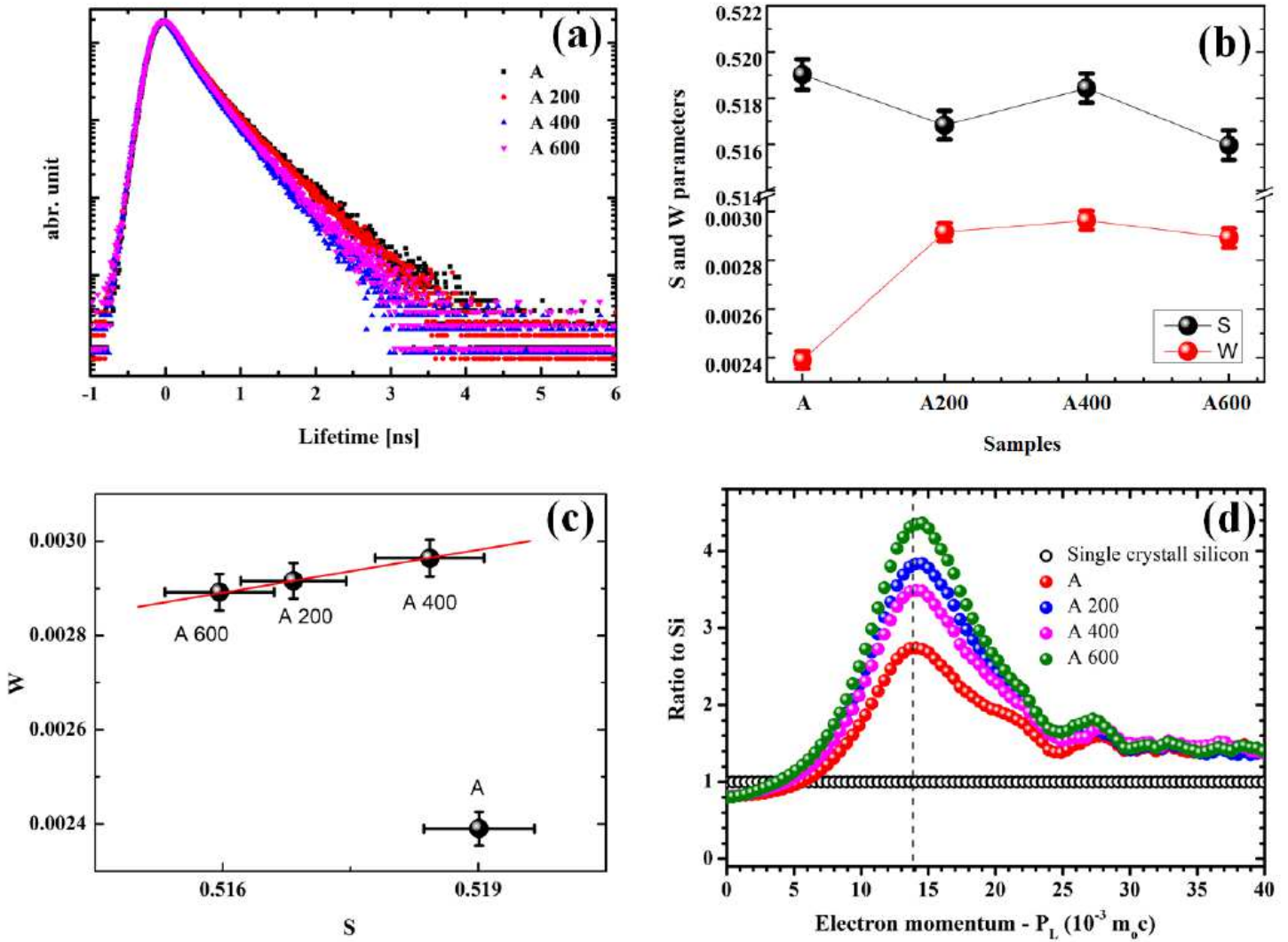


Figure 4

XRD spectra of MnO<sub>x</sub> samples at different temperatures (a) and neutron diffraction spectra of A and A600 samples (b). Lowest vertical red sticks stand for the reference diffraction indices associated with XRD and ND peaks.



**Figure 5**

Positron lifetime spectra (a), S and W parameters of Doppler broadening measurements (b), and correlated plot of S and W parameters (c) for A-A600 samples. (d) Ratio curves of electron momentum distribution of A-A600 samples to a reference pure single-crystal silicon.